Hydrogen evolution by a metal-free electrocatalyst

AUTHOR(S)

Y Zheng, Y Jiao, Y Zhu, Luhua Li, Y Han, Ying (Ian) Chen, A Du, M Jaroniec, S Z Qiao

PUBLICATION DATE

01-01-2014

HANDLE

10536/DRO/DU:30067693

nature COMMUNICATIONS

ARTICLE

Received 12 Nov 2013 | Accepted 2 Apr 2014 | Published 28 Apr 2014

DOI: 10.1038/ncomms4783

Hydrogen evolution by a metal-free electrocatalyst

Yao Zheng[1,2,*], Yan Jiao[1,*], Yihan Zhu[3], Lu Hua Li[4], Yu Han[3], Ying Chen[4], Aijun Du[5], Mietek Jaroniec[6] & Shi Zhang Qiao[1]

Electrocatalytic reduction of water to molecular hydrogen via the hydrogen evolution reaction may provide a sustainable energy supply for the future, but its commercial application is hampered by the use of precious platinum catalysts. All alternatives to platinum thus far are based on nonprecious metals, and, to our knowledge, there is no report about a catalyst for electrocatalytic hydrogen evolution beyond metals. Here we couple graphitic-carbon nitride with nitrogen-doped graphene to produce a metal-free hybrid catalyst, which shows an unexpected hydrogen evolution reaction activity with comparable overpotential and Tafel slope to some of well-developed metallic catalysts. Experimental observations in combination with density functional theory calculations reveal that its unusual electrocatalytic properties originate from an intrinsic chemical and electronic coupling that synergistically promotes the proton adsorption and reduction kinetics.

[1] School of Chemical Engineering, University of Adelaide, Adelaide, South Australia 5005, Australia. [2] Australian Institute for Bioengineering and Nanotechnology, University of Queensland, Brisbane, Queensland 4072, Australia. [3] Physical Sciences and Engineering Division, King Abdullah University of Science and Technology, Thuwal 23955-6900, Kingdom of Saudi Arabia. [4] Institute for Frontier Materials, Deakin University, Waurn Ponds, Victoria 3216, Australia. [5] School of Chemistry, Physics and Mechanical Engineering, Queensland University of Technology, Brisbane, Queensland 4001, Australia. [6] Department of Chemistry and Biochemistry, Kent State University, Kent, Ohio 44242, USA. * These authors contributed equally to this work. Correspondence and requests for materials should be addressed to S.Z.Q. (email: s.qiao@adelaide.edu.au).

Hydrogen evolution reaction (HER), as a fundamental step of electrochemical water splitting and a cornerstone to explore the mechanism of other multi-electron transfer processes in electrocatalysis, always requires a favourable catalyst to achieve fast kinetics for practical applications[1–3]. Among a wide variety of available catalysts, Pt supported on carbon shows unbeatable electrocatalytic HER properties with extremely high exchange current density and small Tafel slope[4]. However, to gain a sustainable hydrogen production, cost-effective alternatives to precious and low abundant Pt catalyst should be developed with high electrocatalytic activities and stabilities[5–8]. Despite tremendous efforts in this direction, all efficient HER electrocatalysts heretofore are based on transition metals, such as Co, Ni, Fe, Mo and their molecular derivatives[7–19], which suffer inherent corrosion susceptibility to the acidic proton exchange membrane electrolysis. A robust catalytic system beyond metals has not been found yet[3,8], largely narrowing the selection range of competitive candidates as Pt's replacements.

Various carbon-based materials feature unique advantages for designated catalysis due to their tunable molecular structures, abundance and strong tolerance to acid/alkaline environments. Very recent advances in low-dimensional carbon materials, as metal-free catalysts, have shown their promising future in energy-related electrocatalytic oxygen reduction and evolution reactions[20–23]. However, this innovative concept has not been explored yet for one of the most important electrolysis processes, hydrogen evolution, due to the poorly known HER mechanism on such materials. So far, all experimental and theoretical studies on the electrocatalytic HER are exclusively focused on the surface properties of metallic catalysts due to the importance of metal–H bonds in this process[3,8]; whether a metal-free material can exhibit similar catalytic behaviour and be more active than metal-based electrocatalysts is still unknown.

In this work, we report the synthesis of a metal-free catalyst, consisting of carbon and nitrogen only, by coupling graphitic-carbon nitride (g-C_3N_4) with nitrogen-doped graphene (*N*-graphene; NG), and demonstrate that the resulting C_3N_4@NG hybrid possesses unique molecular structure and electronic properties for electrocatalytic HER application. This metal-free hybrid shows comparable electrocatalytic HER activity with the existing well-developed metallic catalysts, such as nanostructured MoS_2 materials, although its activity is not as high as that of the state-of-the-art Pt catalyst. Electrochemical measurements in combination with thermodynamic calculations reveal that its unusual electrocatalytic properties originate from a synergistic effect of this hybrid nanostructure, in which g-C_3N_4 provides highly active hydrogen adsorption sites, while N-graphene facilitates the electron-transfer process for the proton reduction. The findings provide clear evidence that, similar to precious metals, the well-designed metal-free counterparts also have great potential for highly efficient electrocatalytic HER, thus opening a new avenue towards replacing noble metals by broader alternatives in a wide variety of applications.

Results

Catalyst synthesis and atomic structure. g-C_3N_4 was grown directly on the surface of chemically exfoliated graphene oxide (GO) films to produce a strong chemical adhesion with the resultant *N*-graphene. GO was thermally reduced with simultaneous nitrogen heteroatom incorporation into framework driven by gaseous NH_3 released during polycondensation of g-C_3N_4's precursor (dicyandiamide) to melem units[24], forming a C_3N_4@NG hybrid (Supplementary Fig. 1). The aberration-corrected high-resolution transmission electron microscopy image of the as-synthesized hybrid shows two-dimensional sheets with complex Moiré patterns, suggesting its multilayered structure formed by stacking multilayered g-C_3N_4 on *N*-graphene sheets (Fig. 1a). It is observed that the g-C_3N_4 phase is less stable than *N*-graphene under electron beam due to the rapid decomposition of its polymeric melon units[25]. After selective removal of g-C_3N_4 layers from the surface of *N*-graphene by transmission electron microscopy irradiation, a residual few-layered *N*-graphene substrate with graphite-like atomic structure was resolved in the identical area of the initial g-C_3N_4-covered sample (Fig. 1b).

Electron microscopy characterization. Scanning transmission electron microscopy combined with electron energy loss spectroscopy (EELS) was used to investigate the C_3N_4@NG hybrid. High-angle-annular-dark-field–scanning transmission electron microscopy revealed that C_3N_4@NG consists of ultra-thin nanosheets with a fairly uniform thickness (Fig. 1e). The spatial distributions of different species in the nanosheet were visualized by EELS mapping based on the intensity variation of their energy loss peaks. Note that unlikely, as in the case of carbon species that are distributed over the entire sheet (Fig. 1f), nitrogen species concentrate in the specific regions (Fig. 1g). These results indicate that *N*-graphene having a low concentration of N (Supplementary Fig. 2) is partially covered by g-C_3N_4 nanodomains on its surface. Figure 1c shows two typical EELS spectra that were collected from g-C_3N_4-containing and g-C_3N_4-free regions (site 1 and site 2 in Fig. 1e), respectively. The fine structures of carbon K-edges are magnified in Fig. 1d, where the two π^* edges at 283.4 eV (peak 1) and 285.5 eV (peak 2) and one σ^* edge at 290.2 eV (peak 3) are attributed to the defective, graphitic and sp^3 carbon species, respectively[26,27]. The EELS mapping with these energy loss peaks reveals that graphitic-sp^2 carbon is present over the entire sheet (Fig. 1i), whereas defective carbon species are only present in the g-C_3N_4-containing regions but absent in the g-C_3N_4-free regions (Fig. 1h) or in a pure g-C_3N_4 sample (Supplementary Fig. 3). These defective species that can be assigned to low-coordinated carbon atoms (26) are probably associated with the breakage of the N–3C bridging bonds at the edge of g-C_3N_4 moieties, due to the strong interaction between g-C_3N_4 and *N*-graphene substrate (Supplementary Fig. 4). In addition, an enhanced intensity of σ^* excitation (peak 3) is observed in the g-C_3N_4-containing region (Fig. 1j), which is indicative of new sp^3 carbon species formed through the growth of g-C_3N_4 nanodomains on the *N*-graphene surface. These observations suggest the generation of chemical bonds between these two materials during coupling process of g-C_3N_4 and *N*-graphene.

NEXAFS and XPS studies. We used Synchrotron-based near-edge X-ray absorption fine structure (NEXAFS) and X-ray photoelectron spectroscopy (XPS) to further probe this interfacial interaction by exploring the lateral structure of C_3N_4@NG multilayered nanosheet. In the carbon K-edge NEXAFS spectra (Fig. 2a), the hybrid shows characteristic resonances of both g-C_3N_4 and *N*-graphene individuals including structural defects at ~284 eV, $\pi^*_{C=C}$ at 285.5 eV and π^*_{C-N-C} at 288.5 eV. In nitrogen K-edge region (Fig. 2b), C_3N_4@NG shows two typical π^* resonances at 399.7 and 402.6 eV corresponding to aromatic C–N–C coordination in one tri-*s*-triazine heteroring (N1, see the inset of Fig. 2b) and N–3C bridging among three tri-*s*-triazine moieties (N2, see the inset of Fig. 2b)[24,25]. As compared with pure g-C_3N_4, a decreased intensity of N2 resonance in the hybrid reveals a partial breaking of N–3C bridgings, which is in agreement with the EELS results. More importantly, as can be seen from the carbon K-edge polarization-dependent NEXAFS spectra (Fig. 2c), a weak shoulder at 287.4 eV (assigned to the π^*

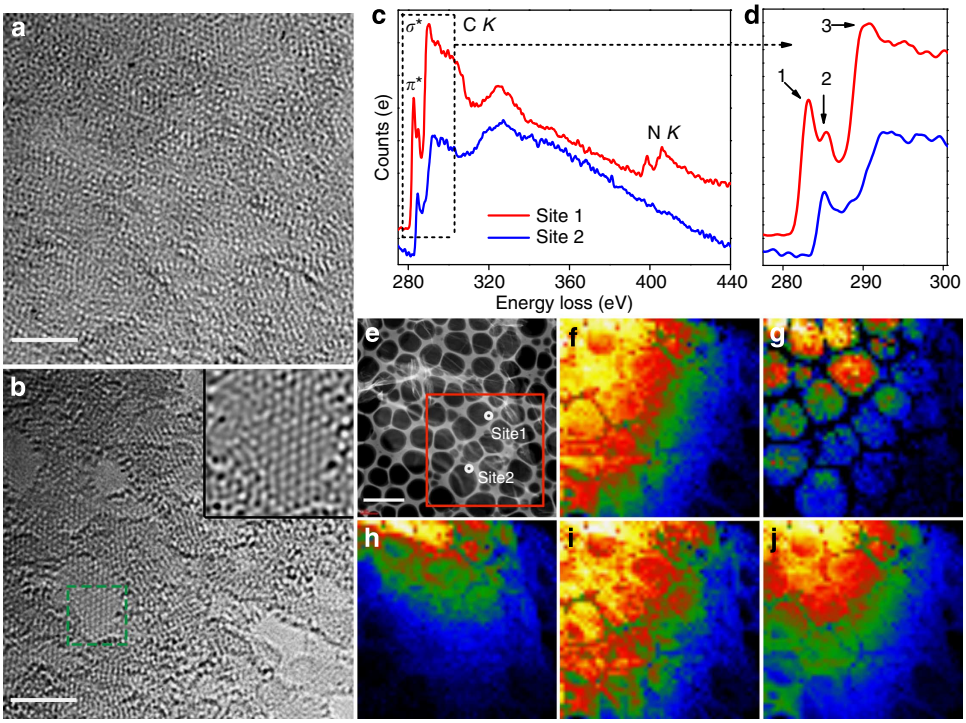

Figure 1 | Electron microscopy characterization of C_3N_4@NG nanosheet. (**a**) Aberration-corrected and monochromated high-resolution transmission electron microscopy image of freshly prepared C_3N_4@NG hybrid. (**b**) High-resolution transmission electron microscopy image of the same area as (**a**) after removal of g-C_3N_4 layer by electron beam irradiation (under a prolonged exposure of ~20 s). Scale bar, 2 nm (**a**,**b**). (**c**) EELS spectra of C_3N_4@NG collected at two specific sites as indicated in **e**. Site 1 represents a g-C_3N_4-containing region with apparent nitrogen K-edge energy loss peak at ~400 eV; site 2 represents a g-C_3N_4-free region. (**d**) Fine structure of the carbon K-edge EELS on C_3N_4@NG. (**e**–**g**), High-angle-annular-dark-field-scanning transmission electron microscopy image of C_3N_4@NG nanosheet and EELS mappings of overall (**f**) carbon and (**g**) nitrogen species in the red-line areas. Scale bar, 2 μm (**e**). (**h**–**j**), EELS mappings of various carbon species (peak 1–3, respectively) as indicated in **d**. A temperature colour code is used in mapping images where the intensity increases as the colour changes in the order of black-blue-green-red-yellow-white.

resonance of C–N species) shows a different angular dependence to the in-plane C–N–C and C = C species, indicating the out-of-plane orientation of new species between g-C_3N_4 and *N*-graphene basals[28]. The XPS spectra also reveal extra sp^3 C–N species at 287.2 eV involved in the *in situ*-formed C_3N_4@NG hybrid[29], which do not exist in a physically mixed g-C_3N_4 and *N*-graphene (C_3N_4/NG) (Fig. 2d). Thus, a combination of polarization-dependent NEXAFS and XPS results provides a crucial evidence for the interfacial interaction model between g-C_3N_4 and *N*-graphene, where the out-of-plane oriented C–N bonds are clearly detected. These interlayer bonds can provide a high interconnectivity between g-C_3N_4 and *N*-graphene parallel layers for a rapid electron transfer to boost hybrid's electrocatalytic activity.

Electronic structure and electron-transfer properties. We conducted density functional theory (DFT) calculations to show the interlayer electronic-coupling effect between g-C_3N_4 and *N*-graphene (Supplementary Figs 5,6). Contrary to the semiconductive pure g-C_3N_4, C_3N_4@NG hybrid shows no band gap due to the downshifting of the Dirac cone at the Γ point to guarantee a fast electron transfer (Fig. 3a). More importantly, after coupling g-C_3N_4 with *N*-graphene, the charge density in hybrid's interlayer was redistributed in the form of an apparent electron transfer from conductive *N*-graphene to g-C_3N_4, leading to an electron-rich region on g-C_3N_4 layer and a hole-rich region on *N*-graphene layer (Fig. 3b). Such localized electron accumulation (0.15 e^- per C_3N_4@NG unit cell) leads to the downshifting of the valance and conduction bands of g-C_3N_4; as a result, the Fermi level crosses the conduction band of g-C_3N_4 as demonstrated by the projected density of states shown in Fig. 3c. This change in projected density of states between pure g-C_3N_4 and hybridized C_3N_4@NG indicates enhanced electron mobility in the latter, which is significant for the electrocatalytic HER.

Electrochemically-measured HER activity. The chemical coupling and concomitant electron's re-distribution between g-C_3N_4 and *N*-graphene can provide a resistance-less path for fast electron transfer through C_3N_4@NG's interlayers and consequently accelerate the electrocatalytic HER kinetics on its surface. The polarization curve (*i*–*V*) recorded on C_3N_4@NG shows an overpotential of ~240 mV to achieve a 10-mA cm^{-2} HER current density and a Tafel slope of 51.5 mV dec^{-1} (Fig. 4a,b, Supplementary Fig. 7). The HER exchange current density (i_0) for C_3N_4@NG, calculated from Tafel plot by extrapolation method, is 3.5×10^{-7} A cm^{-2}; this value is comparable (within an order of magnitude) to those of the well-developed nanostructured MoS_2-based metallic catalysts after normalizing them to the same surface area and catalyst loading (Supplementary Fig. 8, Supplementary Tables 1 and 2)[15,30–32]. Importantly, the interfacial covalent bonds between g-C_3N_4 and *N*-graphene layers can also guarantee a strong molecular framework of the hybrid. Therefore, the C_3N_4@NG catalyst, formed solely from C and N without any metallic elements, features a robust stability in both acidic and alkaline solutions that is required for a sustainable hydrogen production (Fig. 4c). Note that pure g-C_3N_4 and *N*-graphene, used as control samples, show

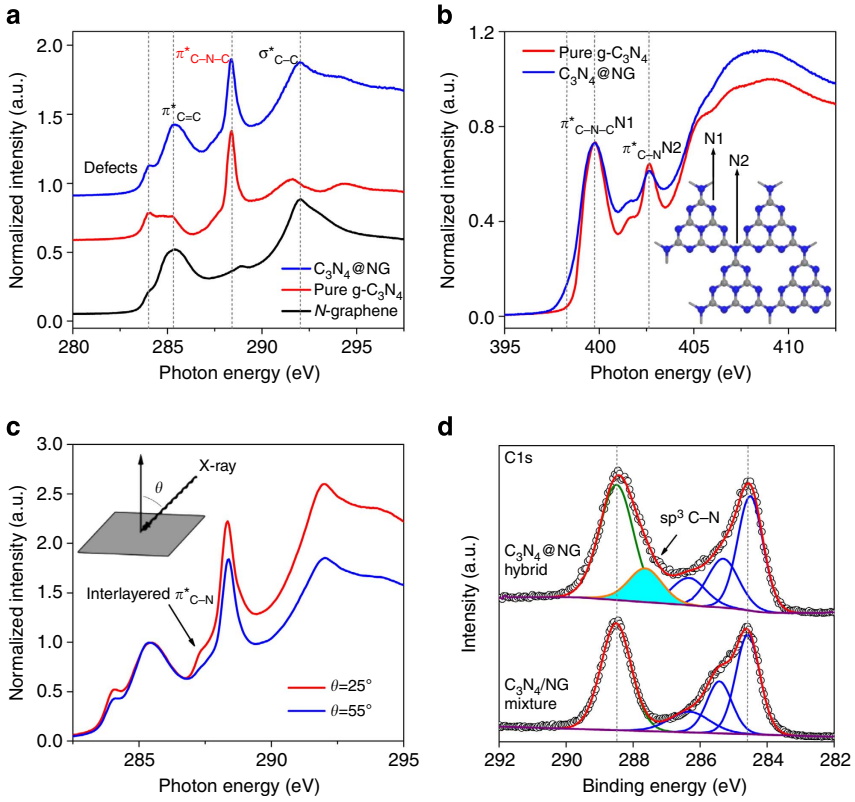

Figure 2 | Chemical structure of C_3N_4@NG. (**a**,**b**) Carbon and nitrogen K-edge NEXAFS spectra of different catalysts. An inset illustrating two types of nitrogen species in g-C_3N_4 molecular network; blue refers nitrogen whereas grey refers carbon atoms. A weaker shoulder on the spectrum of C_3N_4@NG at 398.3 eV is assigned to π^*_{C-N} resonance of nitrogen heteroatom in *N*-graphene. (**c**) Polarization-dependent carbon K-edge NEXAFS spectra of C_3N_4@NG with geometry of the experiment shown in inset. (**d**) High-resolution carbon 1*s* XPS spectra of C_3N_4@NG hybrid and C_3N_4/NG mixture.

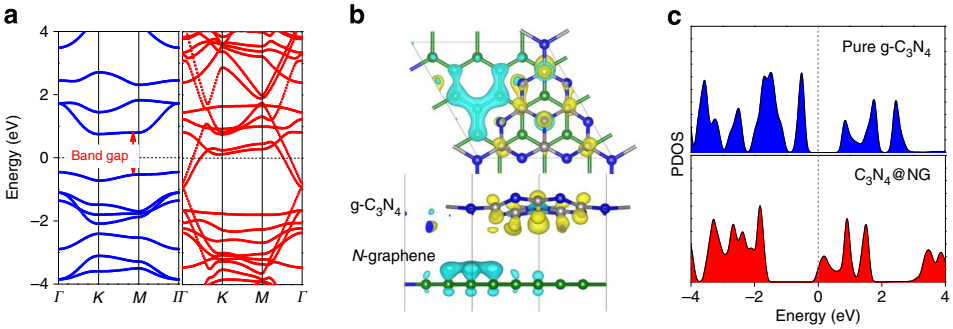

Figure 3 | DFT calculation studies of C_3N_4@NG. (**a**) Band structure of pure g-C_3N_4 (left) and C_3N_4@NG hybrid (right). (**b**) Interfacial electron transfer in C_3N_4@NG. Yellow and cyan iso-surface represents electron accumulation and electron depletion; the iso-surface value is 0.005 e Å^{-3}. (**c**) The projected density of states on pure g-C_3N_4 (top) and C_3N_4@NG hybrid (down).

negligible HER activities due to their nonconductive or nonactive nature, respectively (Fig. 4a). Strikingly, C_3N_4@NG hybrid shows higher proton reduction current than C_3N_4/NG mixture (Supplementary Table 3), unambiguously confirming the critical role of the aforementioned chemical and electronic couplings in achieving an excellent HER activity of the former. Nevertheless, the apparent lower Faradaic resistance in the electrochemical impendence spectrum (Fig. 4d) of *in situ*-formed hybrid, which is related to a charge-transfer process in HER[33], indicates that the enhanced electrocatalytic performance of C_3N_4@NG originates not simply from its increased electrical conductivity because of incorporated conductive *N*-graphene into the hybrid, but from a complex interaction between g-C_3N_4 and *N*-graphene to synergistically promote the HER process.

HER free-energy diagram. We carried out a series of DFT calculations to get a fundamental understanding of the synergistic effect leading to this unexpected high electrocatalytic activity of C_3N_4@NG. In many cases[34–36], the overall HER pathway can be described by a three-state diagram comprising an initial state $H^+ + e^-$, an intermediate adsorbed H*, and a final product ½H_2 (Fig. 5a). The Gibbs free-energy of the intermediate state, $|\Delta G_{H^*}|$, has been considered as a major descriptor of the HER activity for a wide variety of metal catalysts. The optimum value of $|\Delta G_{H^*}|$ should be zero[35]; for instance, this value for the well-known highly efficient Pt catalyst is near-zero as $|\Delta G^{Pt}_{H^*}| \approx 0.09$ eV (Fig. 5a)[35]. Among three metal-free catalysts studied, C_3N_4@NG shows the smallest $|\Delta G_{H^*}|$ value of 0.19 eV (Fig. 5a, Supplementary Fig. 9 and Supplementary Table 4), which is a

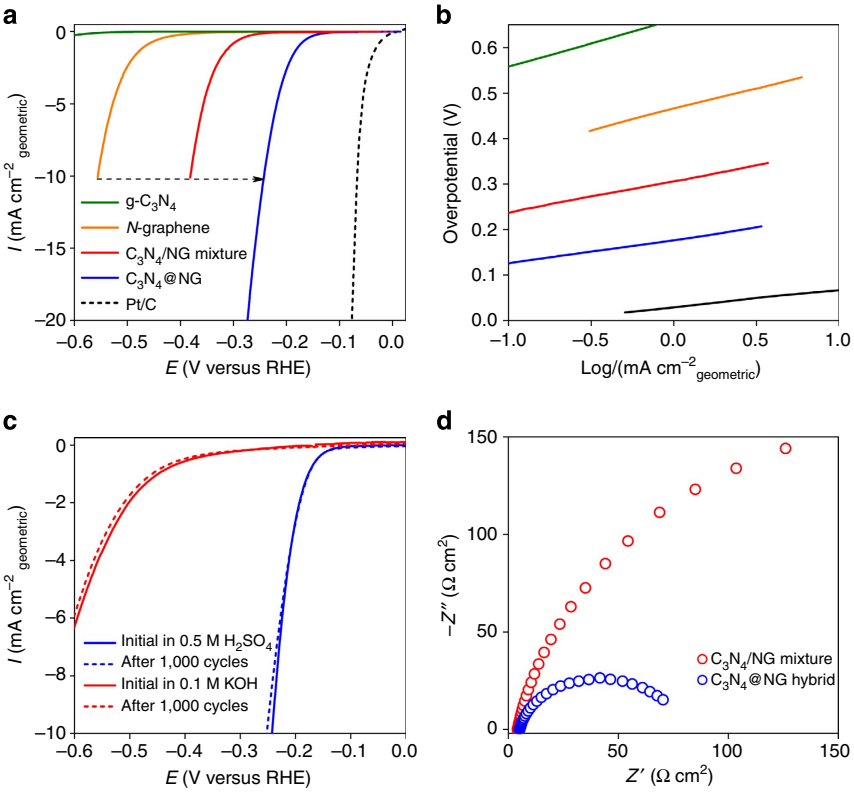

Figure 4 | Fundamental electrochemical relationships measured for HER on C_3N_4@NG. (**a**,**b**) The HER polarization curves and Tafel plots for four metal-free electrocatalysts and 20% Pt/C (electrolyte: 0.5 M H_2SO_4, scan rate: 5 mV s^{-1}). The curve referring to C_3N_4@NG was recorded for the sample with 33 wt% of g-C_3N_4 in the hybrid (see Supplementary Fig. 7 for the performance of the samples with different g-C_3N_4 concentrations). (**c**) Polarization curves recorded for C_3N_4@NG hybrid before and after 1,000 potential sweeps (+0.2 to −0.6 V versus reversible hydrogen electrode) under acidic and basic conditions. (**d**) Electrochemical impedance spectroscopy data for C_3N_4@NG hybrid and C_3N_4/NG mixture in H_2SO_4; data were collected for the electrodes under HER overpotential = 200 mV.

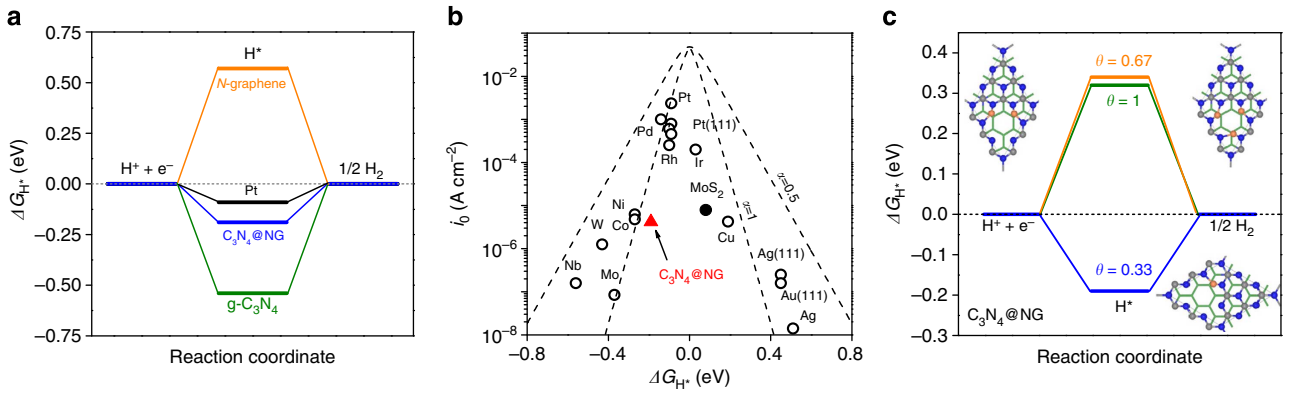

Figure 5 | DFT-calculated HER activities of C_3N_4@NG. (**a**) The calculated free-energy diagram of HER at the equilibrium potential for three metal-free catalysts and Pt reference. (**b**) Volcano plots of i_0 as a function of the ΔG_{H^*} for newly developed C_3N_4@NG (red triangle), common metal catalysts (open symbols, data collected from ref. 35) as well as a typical nanostructured MoS_2 catalyst (closed symbol, data collected from ref. 14). (**c**) Free-energy diagram of HER on the surface of C_3N_4@NG under different H* coverage (1/3, 2/3 and 1 with the molecular configurations shown as insets) conditions.

clear indication of its best electrocatalytic activity from the viewpoint of thermodynamics. Besides, pure g-C_3N_4 and *N*-graphene show reverse ΔG_{H^*} values (Fig. 5a) and H* adsorption behaviours due to their different molecular structures and electronic properties. A largely negative $\Delta G_{H^*} = -0.54$ eV on g-C_3N_4 (Supplementary Fig. 10) indicates that chemical adsorption of H* on its surface is too strong, while a largely positive $\Delta G_{H^*} = 0.57$ on *N*-graphene (Supplementary Fig. 11) indicates very weak H* adsorption and easy product desorption, which both are unfavourable for electrocatalytic HER[36]. However, chemical coupling of g-C_3N_4 and *N*-graphene into a uniform hybrid can result in a mediated adsorption–desorption behaviour ($|\Delta G_{H^*}| \rightarrow 0$) to facilitate the overall HER kinetics, as shown in Fig. 3a. DFT calculations-derived adsorption configuration analysis reveals that such characteristics on C_3N_4@NG surface originates from the unique structure of

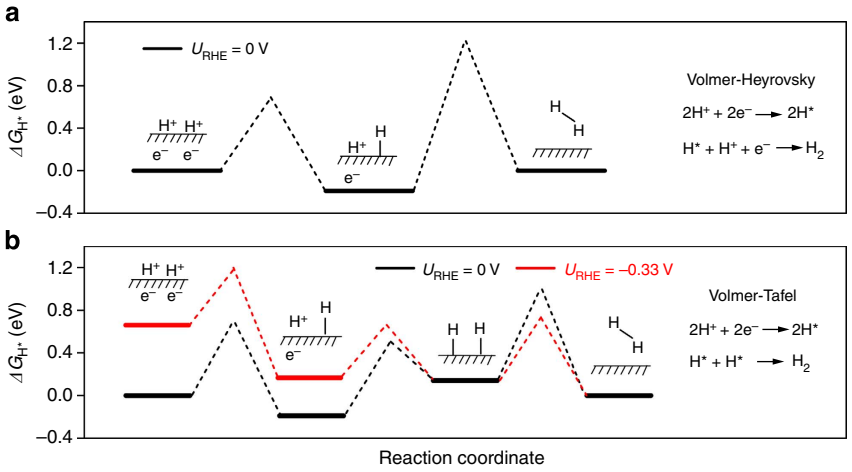

Figure 6 | HER mechanism. Reaction pathways of HER on C_3N_4@NG according to the Volmer–Heyrovsky route (**a**) and Volmer–Tafel route (**b**). Dashed lines are activation barriers for each reaction step as reported elsewhere[37].

g-C_3N_4 molecule allowing one H* bonding with two pyridinic nitrogens in one tri-*s*-triazine periodic unit to form a C_2N_3H heteroring, as illustrated in Supplementary Fig. 9. Simultaneously, a large number of electrons transferred from *N*-graphene to catalytically active g-C_3N_4 layer can rapidly reduce these adsorbed H* species to the final molecular hydrogen. Such atomic-level HER mechanism on the surface of C_3N_4@NG clearly demonstrates the synergistic effect of chemical and electronic couplings on the enhancement of the proton adsorption/reduction kinetics and explains the origin of strikingly high electrocatalytic activity on C_3N_4@NG hybrid.

Volcano plot. The established HER free-energy diagram provides a quantitative relationship between the measured electrochemical activity and theoretical free energy of hydrogen adsorption to further evaluate the electrocatalytic properties of the newly developed C_3N_4@NG in comparison with some typical metallic catalysts. The normalized experimental value of i_0 along with theoretically calculated ΔG_{H^*} for C_3N_4@NG is marked on a volcano-shaped plot shown in Fig. 5b. The catalyst's performance can be quantitatively evaluated by the position of its i_0 and ΔG_{H^*} values relative to the volcano peak (the closer the position of these values to the peak, the better is the catalyst)[36]. As can be seen in Fig. 5b, metal-free C_3N_4@NG catalyst perfectly follows the volcano trend along with a wide collection of metal catalysts, which also validates the predictive capability of the DFT model employed beyond metals. More importantly, the HER activity of the newly developed metal-free electrocatalyst, judged on the basis of both electrocatalytic i_0 and thermodynamic ΔG_{H^*} properties, even surpasses those of the common nonprecious metals and is comparable with that of the state-of-the-art nanostructured MoS_2 electrocatalyst[14,35].

Hydrogen coverage. The DFT calculations further reveal the mechanistic HER behaviour difference on metal-free C_3N_4@NG and traditional metallic catalysts. As shown in Fig. 5c, at low overpotential, one C_3N_4@NG unit cell tends to allow for adsorption of only one H* due to its smallest $|\Delta G_{H^*}|$, yielding a low coverage of $\theta = 1/3$. This structure-oriented low-coverage adsorption of H* on C_3N_4@NG is very different from that on Pt, which is prone to a very high coverage close to $\theta = 1$ (ref. 35). The smaller number of active sites on a certain C_3N_4@NG unit cell is the inherent reason for its relatively low kinetic activity as compared with that of precious Pt-group catalysts. However, as in the case of nanostructured MoS_2 (ref. 15), one can expect that the design of C_3N_4@NG catalysts with largely exposed active sites for favourable hydrogen adsorption would greatly enhance their electrocatalytic HER performances.

HER mechanism. Although kinetics of the Tafel step on the metal surfaces has been studied in great details, the mechanism of HER on the metal-free catalysts is largely unexplored. Therefore, two generally accepted HER mechanisms, Volmer–Heyrovsky and Volmer–Tafel reactions[4], were studied for the new hybrid catalyst. Assuming that there is no extra energy barriers related to the whole process, only the solid lines in Fig. 6 can be taken into account. As regards the Volmer–Tafel mechanism (Fig. 6a), the DFT calculation-derived HER pathway shows that there is a free-energy difference of 0.33 eV for the second-step Tafel reaction under equilibrium potential, which is higher than that of Heyrovsky reaction (0.19 eV, Fig. 6b). Such energy difference can be eliminated at higher overpotential, for example, 0.33 V under which the free energy of the second and third reaction steps is the same (the red line in panel of Fig. 6b). Therefore, the pathway selectivity on C_3N_4@NG is potential-dependent: at low overpotential the Volmer–Heyrovsky mechanism with a rate-limiting step of electrochemical desorption is the most probable, whereas at high overpotential it becomes the Volmer–Tafel mechanism. Simultaneously, there might be extra barriers related to each reaction step as has been shown for Pt surface[37]; the potential-dependent barrier values derived from previously reported Pt surface are depicted as dashed lines in Fig. 6. Under such assumption that C_3N_4@NG possesses the same energy barriers for each reaction step as those on Pt surface, at low overpotentials the Volmer–Tafel mechanism is much faster than the Volmer–Heyrovsky one, and they become equally fast around -1.0 V versus reversible hydrogen electrode.

Discussion

Our study suggests that the chemical coupling of two different layered materials resulted in the formation of a simple, robust and highly efficient metal-free hybrid catalyst, and the electrocatalytic HER performance of which is comparable or even better than that of traditional metallic catalysts. Experimental observations in combination with DFT calculations reveal that its unusual electrocatalytic properties originate from an intrinsic chemical and electronic coupling that synergistically promotes the proton adsorption and reduction kinetics. This finding may shed light

towards replacing noble metals by metal-free counterparts and pave the way for the performance-oriented molecular design of these innovative materials.

Methods

Materials synthesis. C_3N_4@NG hybrid was synthesized by mixing a given amount of dicyandiamide (DCDA) with 250 ml of chemically exfoliated GO dispersion ($\sim$0.5 mg ml^{-1});[38] the mixture was concentrated by rotary evaporation followed by lyophilization. DCDA was deposited on the GO surface by the electrostatic interactions between negatively charged GO and positively charged DCDA during drying process. The collected dark-brown mixture was then annealed under argon atmosphere at 600 °C for 4 h at a heating rate of 4 °C min^{-1} (the sample was wrapped in aluminium foil to avoid melamine sublimation during heating). In our tests, the amount of initial DCDA was selected as 400, 200, 100 and 50 mg; correspondingly, the resultant C_3N_4@NG hybrids were numbered from #1 to #4 with colour changing from dark green to black. Among these four samples, sample #3 with $\sim$33 wt% of g-C_3N_4 showed the best electrocatalytic HER performance (Supplementary Fig. 7); therefore, if no further notification is provided, C_3N_4@NG notation in the paper refers to sample #3.

Imaging and spectroscopic characterization. Aberration-corrected high-resolution transmission electron microscopy imaging was carried out on a FEI Titan G^2 electron microscope equipped with image-corrector operated at 60 kV. A resolution limit of $\sim$1.2 Å was achieved under the imaging conditions used. The scanning transmission electron microscopy imaging and EELS mapping were carried out on a cubed FEI Titan G^2 electron microscope equipped with both a probe-corrector and a monochromator operated at 80 kV. The probe convergence angle was 24.9 mrad and the inner detector angle was 76 mrad. A probe size of 1.5 Å and a best energy resolution of 0.17 eV, as measured from the full-width-at-half-maximum of the zero-loss peak, were achieved. For simultaneous EELS mapping of K-edge structures for carbon and nitrogen, a 2-mm spectrometer entrance aperture and 0.1 eV per channel dispersion were used ($\sim$0.4 eV energy resolution).

The synchrotron-based NEXAFS measurements were carried out on the soft X-ray spectroscopy beamline at the Australian Synchrotron, which is equipped with a hemispherical electron analyser and a microchannel plate detector that enables a simultaneous recording of the total electron yield and partial electron yield. The raw NEXAFS data were normalized to the photoelectron current of the photon beam, measured on an Au grid. The lab-based XPS measurements were performed on a Kratos Axis ULTRA X-ray Photoelectron Spectrometer incorporating a 165-mm hemispherical electron energy analyser. The incident radiation was Monochromatic Al Kα X-rays (1,486.6 eV) at 225 W (15 kV, 15 mA). Survey scans were taken at analyser pass energy of 160 eV and high-resolution scans at 20 eV.

Electrochemical characterization. Considering C_3N_4@NG electrode as an example, the catalyst was ultrasonically dispersed in pure water containing 0.1 wt% of Nafion. Next, 20 µl of catalyst aqueous dispersion (1.0 mg ml^{-1}) were transferred onto the glassy carbon rotating disk electrode (0.196 cm^2) serving as a working electrode. The reference electrode was an Ag/AgCl in 4 M AgCl–KCl solution and the counter electrode was a graphite rod. All potentials were referenced to a reversible hydrogen electrode by adding a value of $(0.205 + 0.059 \times \mathrm{pH})$ V and all polarization curves were corrected for the iR contribution within the cell. A flow of N_2 was maintained over the electrolyte during the experiment to eliminate dissolved oxygen. The working electrode was rotated at 1,600 r.p.m. to remove hydrogen gas bubbles formed at the catalyst surface.

DFT calculations. The electronic structures of all catalysts were computed by Vienna *Ab-initio* Simulation Package (VASP). An all-electron description, the projector-augmented wave method was used to describe the electron–ion interaction. All calculations were performed with PBE exchange-correlation functional (the 1996 functional of Perdew, Burke and Ernzerhof) on periodically repeated slabs. Molecular model-building details, free-energy calculations, HER mechanism and relevant references are given in the Supplementary Methods.

References

1. Lewis, N. S. & Nocera, D. G. Powering the planet: chemical challenges in solar energy utilization. *Proc. Natl Acad. Sci. USA* **103,** 15729–15735 (2007).
2. Turner, J. A. Sustainable hydrogen production. *Science* **305,** 972–974 (2004).
3. Walter, M. G. *et al.* Solar water splitting cells. *Chem. Rev.* **110,** 6446–6473 (2010).
4. Conway, B. E. & Tilak, B. V. Interfacial processes involving electrocatalytic evolution and oxidation of H_2, and the role of chemisorbed H. *Electrochim. Acta.* **47,** 3571–3594 (2002).
5. Subbaraman, R. *et al.* Enhancing hydrogen evolution activity in water splitting by tailoring Li^+-$Ni(OH)_2$-Pt interfaces. *Science* **334,** 1256–1260 (2011).
6. Le Goff, A. *et al.* From hydrogenases to noble metal-free catalytic nanomaterials for H_2 production and uptake. *Science* **326,** 1384–1387 (2009).
7. Zhuo, J. *et al.* Salts of $C_{60}(OH)_8$ electrodeposited onto a glassy carbon electrode: surprising catalytic performance in the hydrogen evolution reaction. *Angew. Chem. Int. Ed.* **52,** 10867–10870 (2013).
8. Cook, T. R. *et al.* Solar energy supply and storage for the legacy and nonlegacy worlds. *Chem. Rev.* **110,** 6474–6502 (2010).
9. Artero, V., Chavarot-Kerlidou, M. & Fontecave, M. Splitting water with cobalt. *Angew. Chem. Int. Ed.* **50,** 7238–7266 (2011).
10. DuBois, M. R. & DuBois, D. L. The roles of the first and second coordination spheres in the design of molecular catalysts for H_2 production and oxidation. *Chem. Soc. Rev.* **38,** 62–72 (2009).
11. Cobo, S. *et al.* A Janus cobalt-based catalytic material for electro-splitting of water. *Nat. Mater.* **11,** 802–807 (2012).
12. Du, P. & Eisenberg, R. Catalysts made of earth-abundant elements (Co, Ni, Fe) for water splitting: recent progress and future challenges. *Energy Environ. Sci.* **5,** 6012–6021 (2012).
13. Popczun, E. J. *et al.* Nanostructured nickel phosphide as an electrocatalyst for the hydrogen evolution reaction. *J. Am. Chem. Soc.* **135,** 9267–9270 (2013).
14. Jaramillo, T. F. *et al.* Identification of active edge sites for electrochemical H_2 evolution from MoS_2 nanocatalysts. *Science* **317,** 100–102 (2007).
15. Kibsgaard, J., Chen, Z., Reinecke, B. N. & Jaramillo, T. F. Engineering the surface structure of MoS_2 to preferentially expose active edge sites for electrocatalysis. *Nat. Mater.* **11,** 963–969 (2012).
16. Voiry, D. *et al.* Enhanced catalytic activity in strained chemically exfoliated WS_2 nanosheets for hydrogen evolution. *Nat. Mater.* **12,** 850–855 (2013).
17. Najmaei, S. *et al.* Vapour phase growth and grain boundary structure of molybdenum disulphide atomic layers. *Nat. Mater.* **12,** 754–759 (2013).
18. Laursen, A. B., Kegnæs, S., Dahla, S. & Chorkendorff, I. Molybdenum sulfides–efficient and viable materials for electro- and photoelectrocatalytic hydrogen evolution. *Energy Environ. Sci.* **5,** 5577–5591 (2012).
19. Merki, D. & Hu, X. Recent developments of molybdenum and tungsten sulfides as hydrogen evolution catalysts. *Energy Environ. Sci.* **4,** 3878–3888 (2011).
20. Gong, K., Du, F., Xia, Z., Durstock, M. & Dai, L. Nitrogen-doped carbon nanotube arrays with high electrocatalytic activity for oxygen reduction. *Science* **323,** 760–764 (2009).
21. Mirzakulova, E. *et al.* Electrode-assisted catalytic water oxidation by a flavin derivative. *Nat. Chem.* **4,** 794–801 (2012).
22. Zhao, Y., Nakamura, R., Kamiya, K., Nakanishi, S. & Hashimoto, K. Nitrogen-doped carbon nanomaterials as non-metal electrocatalysts for water oxidation. *Nat. Commun.* **4,** 2390 (2013).
23. Zheng, Y. *et al.* Nanoporous graphitic-C_3N_4@Carbon metal-free electrocatalysts for highly efficient oxygen reduction. *J. Am. Chem. Soc.* **133,** 20116–20119 (2011).
24. Wang, X. *et al.* A metal-free polymeric photocatalyst for hydrogen production from water under visible light. *Nat. Mater.* **8,** 76–80 (2009).
25. Thomas, A. *et al.* Graphitic carbon nitride materials: variation of structure and morphology and their use as metal-free catalysts. *J. Mater. Chem.* **18,** 4893–4908 (2008).
26. Suenaga, K. & Koshino, M. Atom-by-atom spectroscopy at graphene edge. *Nature* **468,** 1088–1090 (2010).
27. Muller, D. A., Tzou, Y., Raj, R. & Silcox, J. Mapping sp^2 and sp^3 states of carbon at sub-nanometre spatial resolution. *Nature* **366,** 725–727 (1993).
28. Rosenberg, R. A., Love, P. J. & Rehn, V. Polarization-dependent C(K) near-edge x-ray-absorption fine structure of graphite. *Phys. Rev. B* **33,** 4034–4037 (1985).
29. Sheng, Z. *et al.* Catalyst-free synthesis of nitrogen-doped graphene via thermal annealing graphite oxide with melamine and its excellent electrocatalysis. *ACS Nano* **5,** 4350–4358 (2011).
30. Chen, Z. *et al.* Core-shell MoO_3-MoS_2 nanowires for hydrogen evolution: a functional design for electrocatalytic materials. *Nano Lett.* **11,** 4168–4175 (2011).
31. Chen, W. *et al.* Hydrogen-evolution catalysts based on non-noble metal nickel molybdenum nitride nanosheets. *Angew. Chem. Int. Ed.* **51,** 6131–6135 (2012).
32. Merki, D., Vrubel, H., Rovelli, L., Fierro, S. & Hu, X. Fe, Co, and Ni ions promote the catalytic activity of amorphous molybdenum sulfide films for hydrogen evolution. *Chem. Sci.* **3,** 2515–2525 (2012).
33. Li, Y. *et al.* MoS_2 nanoparticles grown on graphene: an advanced catalyst for the hydrogen evolution reaction. *J. Am. Chem. Soc.* **133,** 7296–7299 (2011).
34. Nørskov, J. K., Bligaard, T., Rossmeisl, J. & Christensen, C. H. Towards the computational design of solid catalysts. *Nat. Chem.* **1,** 37–46 (2009).
35. Nørskov, J. K. *et al.* Trends in the exchange current for hydrogen evolution. *J. Electrochem. Soc.* **152,** J23–J26 (2005).
36. Greeley, J., Jaramillo, T. F., Bonde, J., Chorkendorff, I. & Nørskov, J. K. Computational high-throughput screening of electrocatalytic materials for hydrogen evolution. *Nat. Mater.* **5,** 909–913 (2006).

37. Skulason, E. *et al.* Modeling the electrochemical hydrogen oxidation and evolution reactions on the basis of density functional theory calculations. *J. Phys. Chem. C* **114,** 18182–18197 (2010).
38. Li, D., Muller, M. B., Gilje, S., Kaner, R. B. & Wallace, G. G. Processable aqueous dispersions of graphene nanosheets. *Nat. Nanotech.* **3,** 101–105 (2008).

Acknowledgements

This research is financially supported by Australian Research Council (DP1095861, DP130104459). NEXAFS measurements were undertaken on the soft X-ray beamline at Australian Synchrotron. DFT calculations were undertaken on the NCI National Facility systems through the National Computational Merit Allocation Scheme.

Author contributions

S.Z.Q. designed the research. Y.Z. synthesized catalysts and conducted chemical characterizations and electrochemical measurements. Y.J. performed the DFT calculations, assisted by A.D., Y.H.Z. and Y.H. carried out high-resolution transmission electron microscopy imaging. L.H.L. and Y.C. made NEXAFS measurements. All authors discussed and analysed the data. S.Z.Q., Y.Z., Y.J. co-wrote the manuscript with input from M.J. and Y.H.

Additional information

Supplementary Information accompanies this paper at http://www.nature.com/naturecommunications

Competing financial interests: The authors declare no competing financial interests.

Reprints and permission information is available online at http://npg.nature.com/reprintsandpermissions/

How to cite this article: Zheng, Y. *et al.* Hydrogen evolution by a metal-free electrocatalyst. *Nat. Commun.* 5:3783 doi: 10.1038/ncomms4783 (2014).

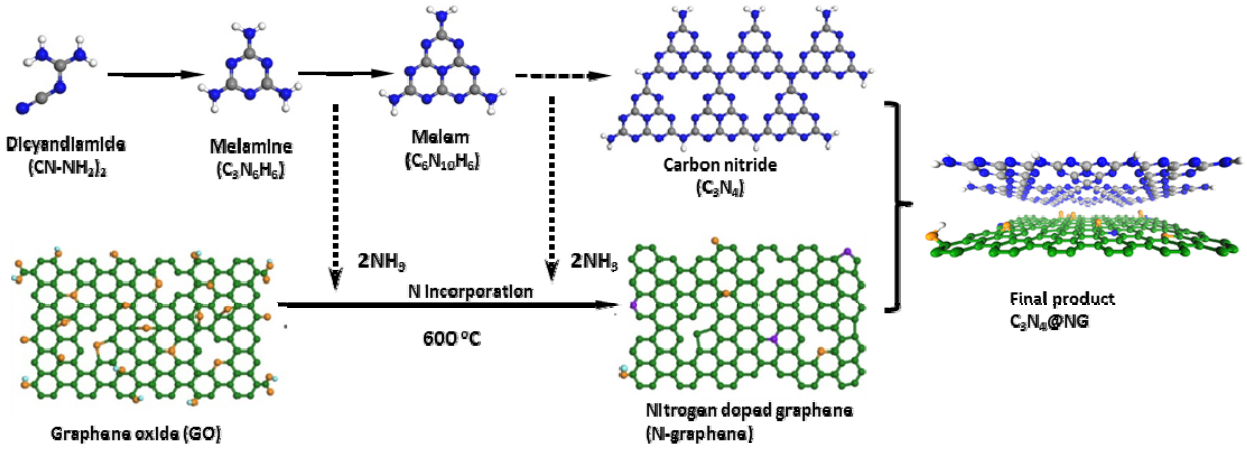

Supplementary Figure 1 Synthesis procedure of C_3N_4@NG hybrid.

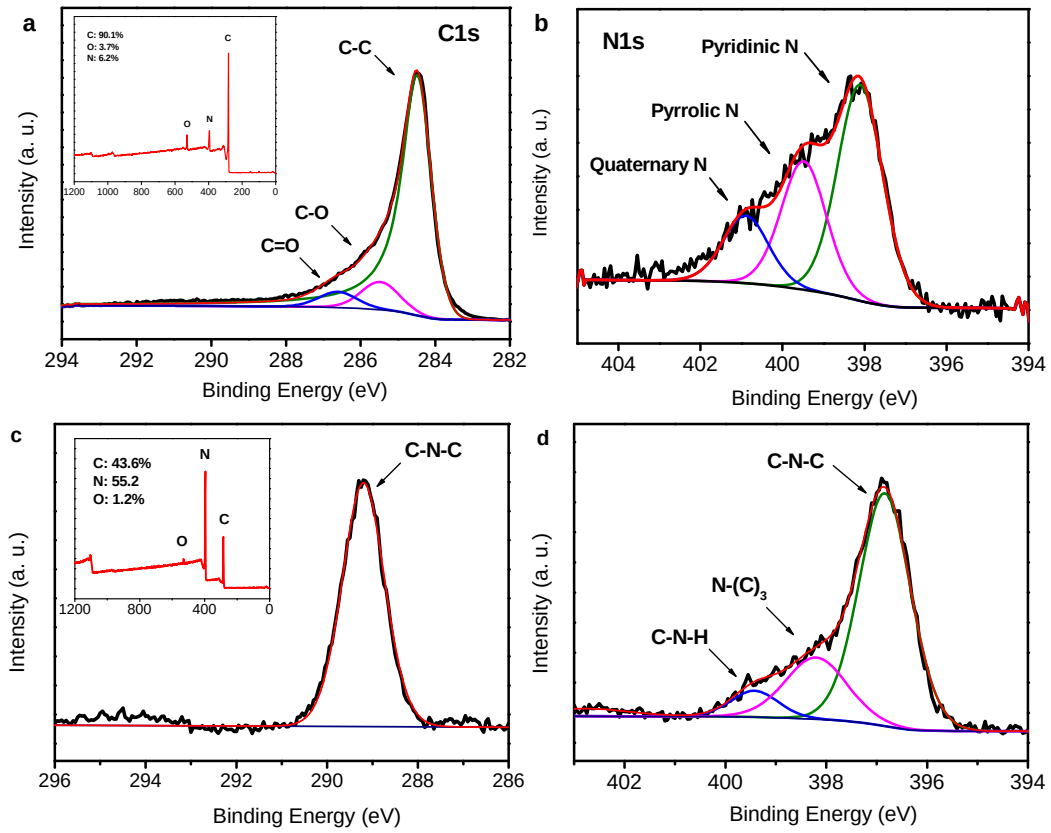

Supplementary Figure 2 (a, b) High-resolution XPS spectra of C1s and N1s in pure N-graphene, which was synthesized by annealing GO powder in 10% NH_3/Ar at 600 ^oC for 4 h. (c, d) High-resolution XPS spectra of C1s and N1s in pure g-C_3N_4, which was prepared by heating melamine in a crucible (with cover) in air at 600 ^oC for 2 h.[1] It is shown that g-C_3N_4's nitrogen concentration is nearly 10 times higher than that of N-graphene.

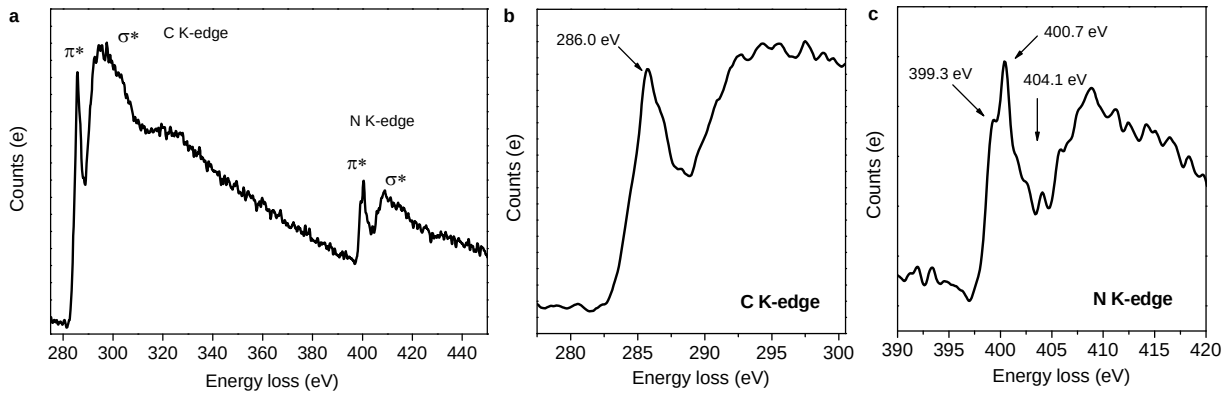

Supplementary Figure 3 EELS spectra of pure g-C_3N_4. The sample shows only one energy-loss peak in carbon K-edge EELS assigned to C-N-C species and three peaks in nitrogen K-edge assigned to C-N-C, C-N and -NH_2/-NH, respectively, from low to high energy-loss.

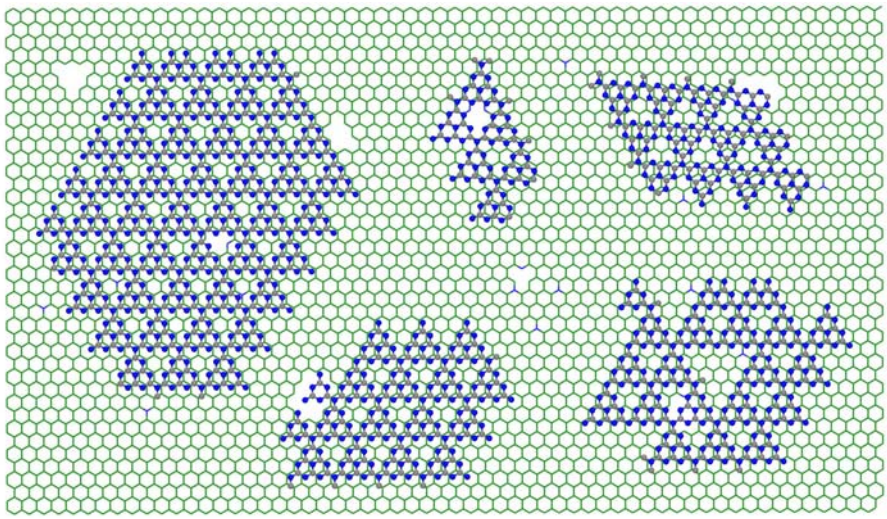

Supplementary Figure 4 Schematic top view of C_3N_4@NG molecular model. Many individual (*poly*)tri-*s*-triazine (C_6N_8) nanodomains with exposed edges are formed on the surface of N-graphene substrate due to the partial breaking of N-3C bridgings during g-C_3N_4 coupling with N-graphene. Green refers to carbon on N-graphene, grey refers to carbon on g-C_3N_4, and blue refers to nitrogen.

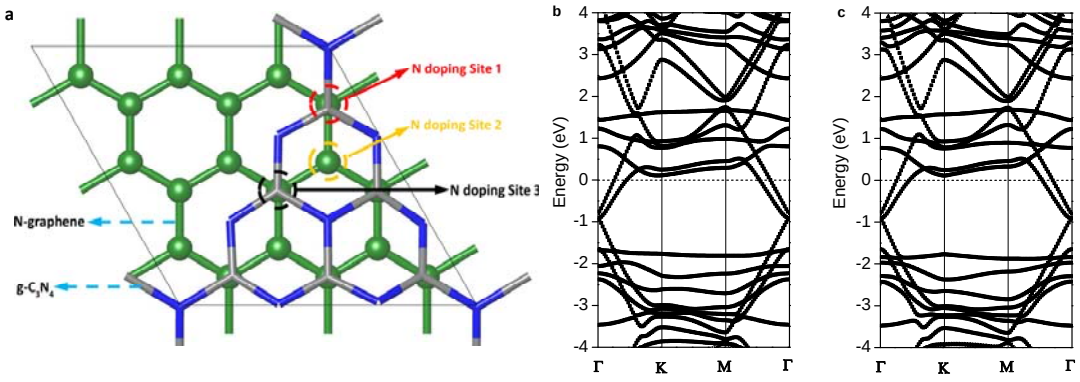

Supplementary Figure 5 Top view of the C_3N_4@NG model with three different doping sites (dashed circles) and corresponding band structures with nitrogen doping site 2 and site 3, respectively. The horizontal dashed lines denote Fermi level. The similar structure of nitrogen doping site 1 in C_3N_4@NG is shown in Figure 3a. Green refers to carbon on graphene, grey refers to carbon on g-C_3N_4, and blue refers to nitrogen on g-C_3N_4.

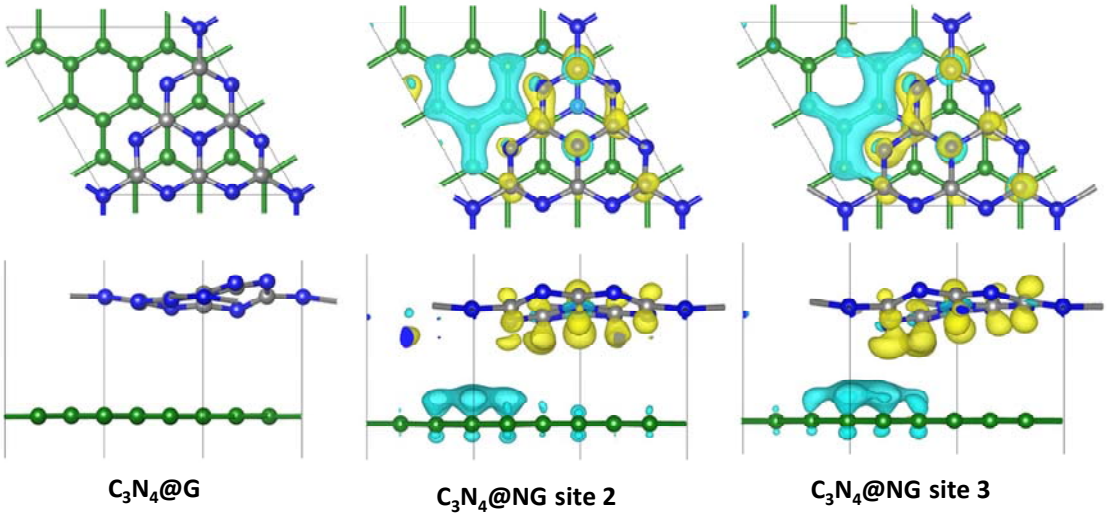

Supplementary Figure 6 Interfacial charge transfer in the case of C_3N_4@G and C_3N_4@NG at the N doping site 2 and site 3. Colour code is the same as that in Supplementary Figure 5. The isosurface value is 0.005 e/Å^3; the electron transfer in C_3N_4@G at such scale is invisible.

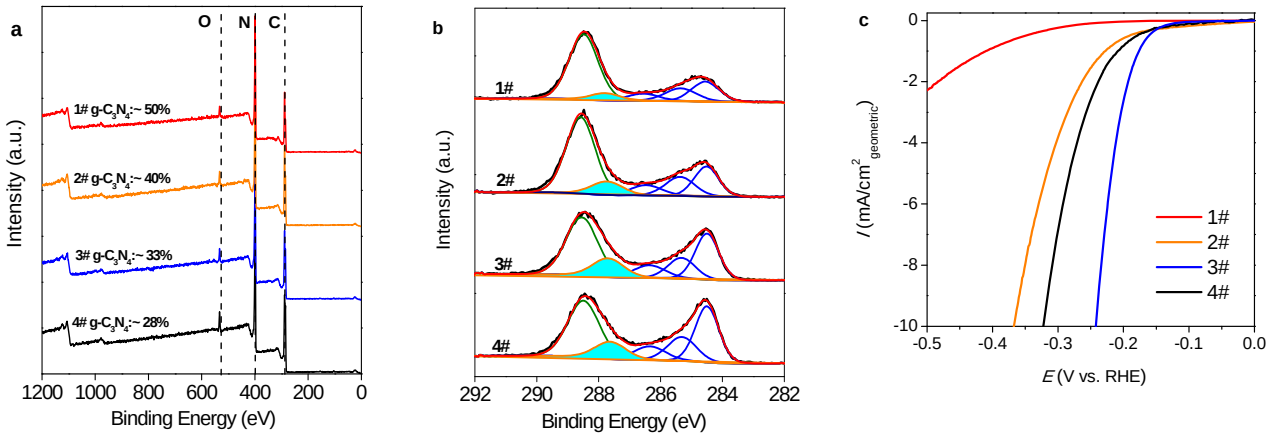

Supplementary Figure 7 (a) XPS survey and (b) high-resolution carbon 1s spectra of different C_3N_4@NG samples prepared using different ratios of initial DCDA and GO. All the samples show chemical interactions between g-C_3N_4 and N-graphene. The amount of g-C_3N_4 is lower than the theoretical value predicted from stoichiometric ratio of the added DCDA due to the melamine sublimation during heating. (c) HER polarization curves recorded for different samples in 0.5 M H_2SO_4. Sample #3 with ~33 wt.% of g-C_3N_4 shows the best activity (lowest overpotential and biggest cathodic current at a certain overpotential); too much g-C_3N_4 or N-graphene reduces the HER activity of the hybrid due to its non-conductive or non-active nature, respectively.

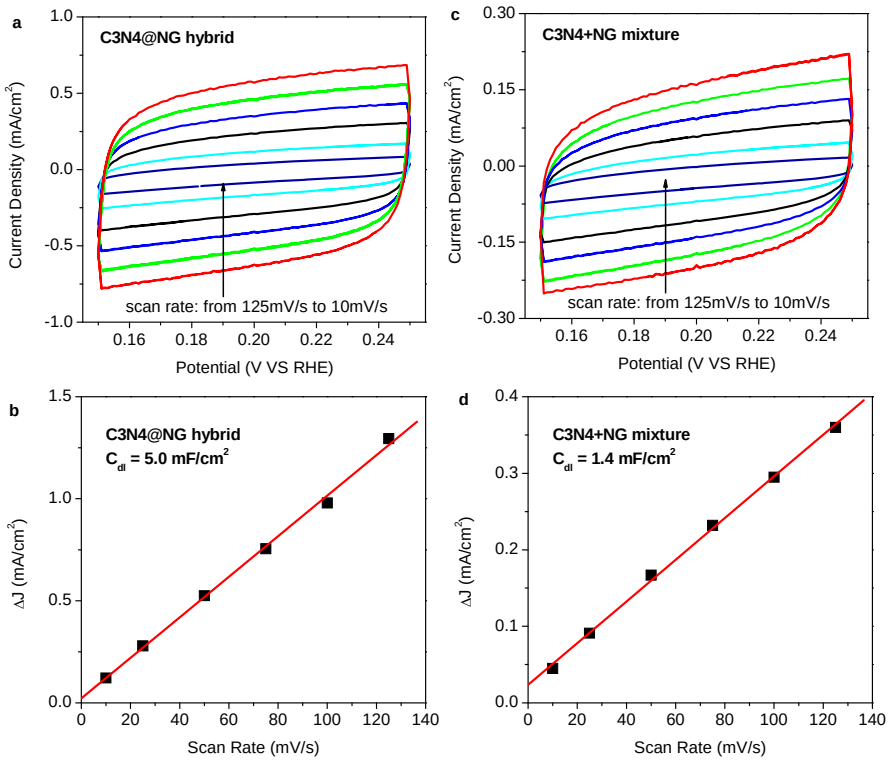

Supplementary Figure 8 (a,c) CV curves and (b,d) the corresponding difference in the current density at 0.2 V plotted against scan rate; the calculated C_{dl} values are shown in insets.

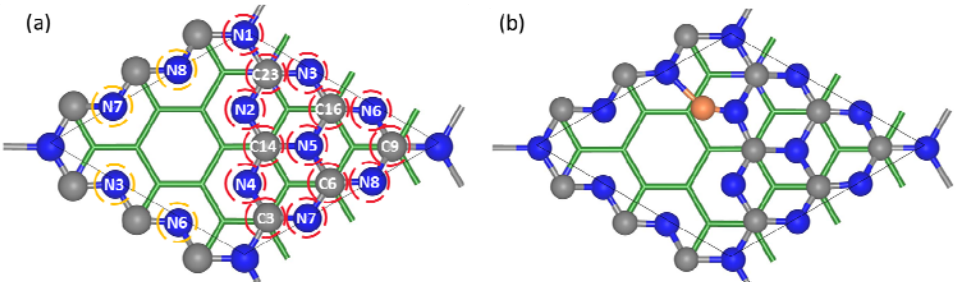

Supplementary Figure 9 (a) Possible H* adsorption sites (highlighted by red circles) on C_3N_4@NG; yellow circles denote the equivalent atoms. The nitrogen doping site on graphene is beneath C23. (b) The most stable H* adsorption pattern on N2. Colour code is the same as Supplementary Figure 5.

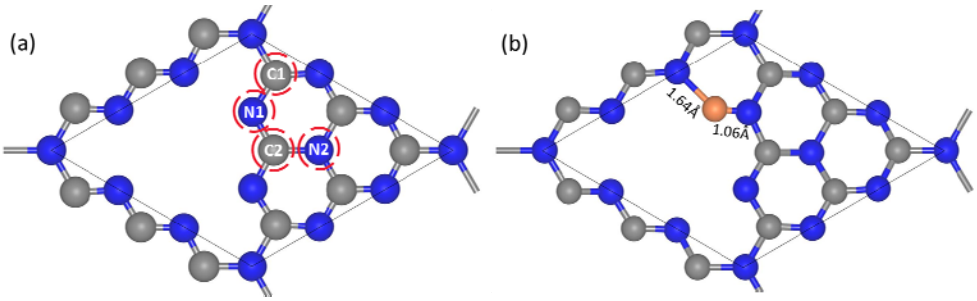

Supplementary Figure 10 (a) Possible H* adsorption sites and (b) the most stable adsorption pattern on pure g-C_3N_4. The ΔG_{H^*} on each of the investigated atoms are: 1.04 eV (C1), -0.53 eV (N1), 1.38 eV (C2), and 1.47 eV (N2). The H* adsorption configuration on pure g-C_3N_4 is the same as that on C_3N_4@NG with a much larger $|\Delta G_{H^*}|$. Colour code is the same as Supplementary Figure 5.

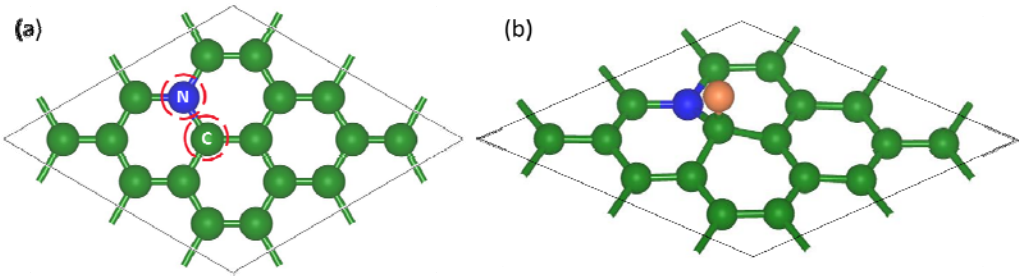

Supplementary Figure 11 (a) Possible H* adsorption sites and (b) the most stable adsorption pattern on pure N-graphene with ΔG_{H^*}=0.57 eV.

Supplementary Table 1 Values of the catalyst loading, electrochemical active surface area, and exchange current density for the currently reported MoS_2-based HER catalysts

Catalyst	catalyst loading ($\mu g/cm^2$)	C_{dl} (mF/cm^2)	I_0 (A/cm^2)	Ref
MoS_2 nanosheet	285	33.7	12.6×10^{-6}	2
MoS_2/graphene	210	10.4	3×10^{-6}	3
Amorphous MoS_3	~31	2.3	8.9×10^{-7}	4
MoO_3-MoS_2 nanowire	60	2.2	0.82×10^{-7}	5
Nanostructured MoS_2	60	4.8	6.9×10^{-7}	6
Nanostructured MoS_2	60	1.1	1.3×10^{-7}	6
Nanostructured MoS_2	60	2.7	2.6×10^{-7}	6
C_3N_4@NG hybrid	100	5.0	3.5×10^{-7}	This work
C_3N_4+NG mixture	100	1.4	2.5×10^{-8}	This work

Supplementary Table 2 Exchange current densities normalized in relation to the catalyst loading and/or active surface area for various catalysts

Catalyst	I_0' (A/cm^2) normalized by mass	I_0' (A/cm^2) normalized by area	C_{dl}' (mF/cm^2) normalized by mass	I_0' (A/cm^2) normalized by mass and area
MoS_2	4.4×10^{-6}	1.9×10^{-6}	11.8	5.3×10^{-6}
MoS_2/graphene	1.4×10^{-6}	1.44×10^{-6}	4.95	3.0×10^{-6}
MoS_3	2.9×10^{-6}	1.93×10^{-6}	7.42	0.6×10^{-6}
MoO_3-MoS_2	0.14×10^{-6}	0.19×10^{-6}	3.67	0.11×10^{-6}
MoS_2	1.2×10^{-6}	0.71×10^{-6}	8.00	0.43×10^{-6}
MoS_2	0.22×10^{-6}	0.59×10^{-6}	1.83	0.35×10^{-6}
MoS_2	0.45×10^{-6}	0.48×10^{-6}	4.50	0.29×10^{-6}
C_3N_4@NG hybrid	0.35×10^{-6}	0.35×10^{-6}	5.0	0.35×10^{-6}
C_3N_4+NG mixture	0.025×10^{-6}	0.089×10^{-6}	1.4	0.089×10^{-6}

Supplementary Table 3 Electrochemical analysis of different catalysts based on the polarization curves and Tafel plot.

Catalyst	η @10mA/cm^2 (V, *vs.* RHE)	Tafel slope (mV/dec)	i_0[a] (A/cm^2)	*Normalized* i_0 in relation to catalyst loading and surface area[b]	*Normalized* i_0 according to eqs. 7-10[c]
C_3N_4@NG	-0.24	51.5	$3.5*10^{-7}$	$3.5*10^{-7}$	$4.4*10^{-6}$
C_3N_4/NG	-0.38	67.0	$2.5*10^{-8}$	$8.9*10^{-8}$	$3.1*10^{-7}$

[a] The exchange current density (i_0) was calculated by extrapolation method.

[b] See Supplementary Table 1,2 for details of the normalization process; normalization was performed in relation to the catalyst loading and surface area.

[c] The i_0 was normalized according to Eqs. 7-11 by using the experimental exchange current density.

Supplementary Table 4 Adsorption energy, free energy, and bond length of H* on C_3N_4@NG complex.

Adsorption Site	ΔE_{H^*} (eV)	ΔG_{H^*}(eV)	H-C/H-N bond length (Å)
N1	1.85 eV	2.09 eV	1.03
N2	-0.43 eV	-0.19 eV	1.07 (1.62[a])
N3	-0.43 eV	-0.19 eV	1.06 (1.63 [a])
N4	-0.37 eV	-0.13 eV	1.07 (1.56 [a])
N5	1.15 eV	1.39 eV	1.03
N6	-0.36 eV	-0.12 eV	1.07 (1.58 [a])
N7	-0.38 eV	-0.15 eV	1.07 (1.59 [a])
N8	-0.40 eV	-0.16 eV	1.07 (1.59 [a])
C23	0.50 eV	0.74 eV	1.11
C14	0.97 eV	1.21 eV	1.12
C16	0.96 eV	1.20 eV	1.12
C3	0.72 eV	0.96 eV	1.11
C6	0.87 eV	1.11eV	1.11
C9	0.72 eV	0.96 eV	1.11

[a] values in parenthesis refer to the second H-N bond.

Supplementary Methods

Experimental Section

Activity normalization

To normalize the activity in relation to the surface area and catalyst loading for newly developed metal-free catalysts, first we calculated the electrochemical active surface areas for the synthesized catalysts by measuring their electrochemical double layer capacitances (C_{dl}) using a simple CV method. It is known that C_{dl} value is expected to be linearly proportional to the electrochemically active surface area of the electrode. A potential range of 0.15-0.25 V vs RHE was selected for the capacitance measurements because no obvious electrochemical features corresponding to the Faradic current were observed in this region for each catalyst (Supplementary Figure 8a,c). Then, the capacitive currents, i.e. $\Delta J_{|Ja-Jc|}$@0.2 V were plotted as a function of the CV scan rate, as shown in Supplementary Figure 8b,d; the linear relationships were observed with the slopes twice larger than the C_{dl} value. According to this method, the C_{dl} values for C_3N_4@hybrid and C_3N_4+NG mixture were calculated to be 5.0 and 1.4 mF/cm^2, respectively.

To compare the normalized activities of C_3N_4@NG, C_3N_4+NG mixture and other metal electrocatalysts (for example, nanostructured MoS_2 material, which is the most often studied HER catalyst), we collected the values of catalyst loading, electrochemical active surface area, and exchange current density for the reported MoS_2-based HER catalysts and summarized in Supplementary Table 1. Assuming the value of the catalyst loading or surface area for C_3N_4@NG hybrid as a reference (kept unchanged), the relative exchange current densities for other metallic electrocatalysts are shown in Supplementary Table 2 (the first and second columns refer to the mass and area normalizations, respectively). By considering the influence of the catalyst loading on the electrochemical active surface area for one catalyst (third column of Supplementary Table 2), it is more reasonable to normalize the exchange current densities to both mass and surface area as shown in the fourth column of

Supplementary Table 2, where one can see that the activity of C_3N_4@NG is "comparable" to those of the well-developed nanostructured MoS_2-based metallic catalysts (within an order of magnitude) and ~four times higher than that of C_3N_4+NG mixture.

Computational Section

General

The electronic structures of all catalysts were computed by Vienna Ab-initio Simulation Package (VASP)[7,8]. An all-electron description, the projector-augmented wave method was used to describe the electron-ion interaction[9,10]. All calculations were performed with PBE exchange-correlation functional on periodically repeated slabs [11,12].

Molecular models and band structures of C_3N_4@NG

The slab model of C_3N_4@NG was established based on a published g-C_3N_4@graphene (C_3N_4@G) hybrid model[13] by replacing one of the carbon atoms in graphene with nitrogen atom in three different doping sites, as shown in Supplementary Figure 5a. The dimension of such a unit cell is 7.14 Å × 7.14 Å × 20 Å with sufficient vacuum space in Z direction to separate the interaction between periodic images. Note that in the performed calculations, only one periodical unit of g-C_3N_4 along N-graphene substrate was considered, while the interlayer C-N bond proved by the EELS and NEXAFS results was not constructed. A Gamma centred 10×10×1 K-point mesh was used to sample the Brillouin zone for geometry optimization, and 40 K-points along each high-symmetry line in the Brillouin zone were used to obtain band structures (Supplementary Figures 5b, c). The cut-off energies for plane waves were chosen to be 500 eV, and the convergence tolerance of force on each atom during structure relaxation was set to be 0.001 eV/Å. Polarization effect was considered in all cases.

Charge transfer between g-C_3N_4 layer and N-graphene layer

The interaction between g-C_3N_4 and N-graphene can be evaluated by the interfacial adhesion energies ($E_{adhesion}$) defined as

$$E_{adhesion} = E_{total} - E_{NG} - E_{g\text{-}C3N4} \quad (4)$$

where E_{total}, E_{NG}, and $E_{g\text{-}C3N4}$ represent the total energy of the C_3N_4@NG hybrid, N-graphene, and g-C_3N_4 monolayer, respectively. The $E_{adhesion}$ of C_3N_4@G is -0.03 *eV,* while the value becomes more negative, as -0.11 *eV*, -0.09 *eV* and -0.10 *eV* for 1, 2 and 3 doping-site models of C_3N_4@NG, respectively, indicating a stronger interaction between g-C_3N_4 and N-graphene due to nitrogen doping into graphene. The Bader[14] charge analysis also suggests an enhanced charge transfer through graphene layer to g-C_3N_4 layer from 0.003 e^- on C_3N_4@G to 0.153 e^-, 0.157 e^-, and 0.156 e^- on 1, 2, 3 doping-site models of C_3N_4@NG, respectively. Three-dimensional electron density difference plots (Supplementary Figure 6) also show that nitrogen incorporation into graphene layer leads to a larger electron transfer to the g-C_3N_4 layer. Note that the different type of N doping site does not influence the electronic structures of different doping patterns and electron transfer phenomena. Therefore, if no further notification is provided, any discussion about doping sites in C_3N_4@NG simply refers to N doping at site 1.

Active sites and adsorption properties

The free energy of the adsorbed state is calculated as

$$\Delta G_{H^*} = \Delta E_{H^*} + \Delta E_{ZPE} - T\Delta S \quad (5)$$

where ΔE_{H^*} is the hydrogen chemisorption energy (either integral or differential), and ΔE_{ZPE} is the difference corresponding to the zero point energy between the adsorbed state and the gas phase. As the vibrational entropy of H* in the adsorbed state is small, the entropy of adsorption of ½ H_2 is $\Delta S_H \approx -½S^0_{H2}$, where S^0_{H2} is the entropy of H_2 in the gas phase at the standard conditions. Therefore the overall corrections are taken as in[15]

$\Delta G_{H^*} = \Delta E_{H^*} + 0.24\ eV$ (6)

The exploration of HER active sites in C_3N_4@NG was conducted by placing a hydrogen atom 1.5 Å above each atom on the g-C_3N_4 layer as shown in Supplementary Figure 9a; the corresponding adsorption energy and free energy of hydrogen adsorption on each atom are shown in Supplementary Table 4.

Exchange current density normalization for volcano-shaped diagram

The exchange current for a certain electrocatalytic process can be calculated by

$$i_0 = Fk^0 C_O^{1-\alpha} C_R^{\alpha} \quad (7)$$

where F is the Faraday constant, α is the transfer coefficient, which is a measure of the symmetry of the energy barrier, k^0 is the standard rate constant as 200 $s^{-1}site^{-1}$ [16], C_O is the surface concentration of oxidant O and C_R is the surface concentration of reductant R in the reaction $O + e^- \rightarrow R$. Simultaneously, the bulk concentration of C_O* and C_R* could be related by K as

$$K = \frac{C_R}{C_O} = \frac{C_R^*}{C_O^*} = \exp[-\frac{1}{k_B T}\Delta G_{H^*}] \quad (8)\#$$

Then the coverage θ for intermediate H*can be expressed by

$$\theta = \frac{C_R}{C_{total}} = \frac{K}{1+K} \quad (9)$$

where C_{total} is the sum of C_o and C_R, i.e. the total number of active sites. Therefore, the exchange current density can be calculated as

$$i_0 = Fk^0 C_{total}[(1-\theta)^{1-\alpha}\theta^{\alpha}] \quad (10)$$

where the pre-factor $\tilde{i}_k = Fk^0 C_{total}$ is calculated as:

$$\tilde{i_k} = Fk^0 C_{total} = ek^0 \frac{N_{sites}}{A} \quad (11)$$

where e is the electric charge per electron, and N_{sites}/A is the number of sites per surface area. According to this equation, the pre-factor is calculated as 7.7 mA cm^{-2} for C_3N_4@NG (i.e. $\tilde{\imath}_{k(C3N4@NG)}$), while its value for Pt(111) is 48 mA cm^{-2}(i.e. $\tilde{\imath}_{k(Pt)}$), as reported elsewhere[12]. Additionally, if the electrochemical active surface areas for Pt and C_3N_4@NG are similar (i.e. at the same order of magnitude), the exchange current density for C_3N_4@NG ($\tilde{\imath}_{k(C3N4@NG)}$) can be normalized by changing $\tilde{\imath}_k$ to the value of Pt(111) ($\tilde{\imath}_{k(Pt)}$). Then, $i_{0(normalized)} = i_{0(measured)} \times \tilde{\imath}_{k(Pt)} / \tilde{\imath}_{k(C3N4@NG)}$. The same normalization method has been also applied for nanostructured MoS_2 electrocatalysts[17]. Note that different with MoS_2 for which only atoms at the edge of each individual island exhibit catalytic activity, the complete g-C_3N_4 lattice shows HER activity with the nitrogen adjacent voids as the active centers.

Study of HER mechanism on C_3N_4@NG

Different number of hydrogen atoms could adsorb within one unit cell and lead to different coverage. An integral adsorption energy, which represents the average adsorption energy per adsorbed hydrogen atom, can then be defined as:

$$\Delta E_{H^*}^{\text{int}} = \frac{1}{n}[E(surf + nH^*) - E(surf) - \frac{n}{2}E(H_2)] \qquad (12)$$

where *n* is the number of H atoms adsorbed on the surface. For C_3N_4@NG, the number of total active sites is estimated on the basis that each adsorbed hydrogen bonds to two pyridinic nitrogen atoms. Hence n=1 corresponds to a coverage of 1/3, while n=3 corresponds to a coverage of 1. From $\Delta E_{H^*}^{\text{int}}$, the differential adsorption energy ($E_{H^*}^{diff}$), which describes the explicit energy needed to increase the coverage by one hydrogen atom can be calculated as:

$$\Delta E_{H^*}^{diff} = E(surf + nH^*) - E[surf + (n-1)H^*] - 1/2E(H_2) \qquad (13)$$

Supplementary References

(1) Thomas, A. *et al*., Graphitic carbon nitride materials: variation of structure and morphology and their use as metal-free catalysts. *J. Mater. Chem.* **18**, 4893–4908 (2008).

(2) Xie, J. *et al.*, Controllable disorder engineering in oxygen-incorporated MoS_2 ultrathin nanosheets for efficient hydrogen evolution. *J. Am. Chem. Soc.* **135**, 17881−17888 (2013).

(3) Liao, L. *et al.*, MoS_2 Formed on mesoporous graphene as a highly active catalyst for hydrogen evolution. *Adv. Funct. Mater.* **23**, 5326–5333 (2013).

(4) Merki, D., Vrubel, H., Rovelli, L., Fierroa, S., & Hu, X. Fe, Co, and Ni ions promote the catalytic activity of amorphous molybdenum sulfide films for hydrogen evolution, *Chem. Sci.* **3**, 2515–2525 (2012).

(5) Chen, Z. *et al.*, Core–shell MoO_3–MoS_2 nanowires for hydrogen evolution: a functional design for electrocatalytic materials. *Nano Lett.* **11**, 4168–4175 (2011).

(6) Kibsgaard, J., Chen, Z., Reinecke, B. N. & Jaramillo, T. F. Engineering the surface structure of MoS2 to preferentially expose active edge sites for electrocatalysis. *Nat Mater.* **11**, 963–969 (2012).

(7) Kresse, G., & Furthmuller, J., Efficiency of ab-initio total energy calculations for metals and semiconductors using a plane-wave basis set. *Comput. Mater. Sci.* **6**, 15–50 (1996).

(8) Kresse, G., & Furthmuller, J., Efficient iterative schemes for ab initio total-energy calculations using a plane-wave basis set. *Phys. Rev. B* **54**, 11169–11186 (1996).

(9) Blochl, P. E., Projector augmented-wave method. *Phys. Rev. B* **50**, 17953–17979 (1994).

(10) Kresse, G. & Joubert, D. From ultrasoft pseudopotentials to the projector augmented-wave method. *Phys. Rev. B* **59**, 1758–1775 (1999).

(11) Perdew, J. P., Burke, K., & Ernzerhof, M., Generalized gradient approximation made simple. *Phys. Rev. Lett.* **77**, 3865–3868 (1996).

(12) Perdew, J. P., Burke, K., & Ernzerhof, M., Erratum: Generalized gradient approximation made simple. *Phys. Rev. Lett.* **78**, 1396 (1997).

(13) Du, A. *et al.*, Hybrid graphene and graphitic carbon nitride nanocomposite: gap opening, electron–hole puddle, interfacial charge transfer, and enhanced visible light response. *J. Am. Chem. Soc.* **137**, 4393–4397 (2012).

(14) Tang, W., Sanville, E., & Henkelman, G., A grid-based Bader analysis algorithm without lattice bias. *J. Phys.: Condens. Matter* **21**, 084204 (2009).

(15) Nørskov, J. K. *et al.*, Trends in the exchange current for hydrogen evolution. *J. Electrochem. Soc.* **152,** J23–J26 (2005).

(16) Nørskov, J. K. *et al*., Origin of the overpotential for oxygen reduction at a fuel-cell cathode. *J. Phys. Chem. B* **108**, 17886–17892 (2004).

(17) Jaramillo, T. F. *et al*., Identification of active edge sites for electrochemical H_2 evolution from MoS_2 nanocatalysts. *Science* **317**, 100–102 (2007).